International Journal of Multiphase Flow 170 (2024) 104625

Contents lists available at ScienceDirect

International Journal of Multiphase Flow

journal homepage: www.elsevier.com/locate/ijmulflow

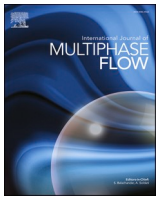

Simulation of multiphase flow in pipes with simplified models of deposited beds

Min Liu (刘敏)[a], Lee F. Mortimer [b,*], Bisrat Wolde [b], Michael Fairweather [b], Yanlin Zhao (赵彦琳)[a], Jun Yao (姚军)[a]

[a] Beijing Key Laboratory of Process Fluid Filtration and Separation, College of Mechanical and Transportation Engineering, China University of Petroleum-Beijing, Beijing 102249, PR China
[b] School of Chemical and Process Engineering, University of Leeds, Leeds, LS2 9JT, United Kingdom

ARTICLE INFO

Keywords:
Turbulent pipe flows
Deposited beds
Lagrangian particle tracking
Secondary flows

ABSTRACT

Turbulent particle-laden flows in pipes can result in particle deposition leading to the formation of solid beds. The presence of such beds modifies the flow field, resulting in secondary motions in the plane of the pipe cross-section, which in turn impact particle transport. In this work turbulent pipe flows with equal mass flow rates and solid beds of height $H_b = 0$ (full pipe), $0.5R$ (three-quarter pipe), and R (half pipe) are predicted using direct numerical simulation, with the beds represented simplistically as flat surfaces. The particulate phase is one-way coupled to the flow at a volume fraction of 10^{-3} and particle motion is solved for using a Lagrangian point-particle approach. The Reynolds numbers computed based on bulk velocity and equivalent pipe diameter for the full, ¾ and, ½ pipes are 5,300, 5,909 and 7,494, respectively. The same particle size is used in all the simulations and their respective Stokes numbers, based on the shear timescale, are 0.5, 1.2 and 1.9, respectively. The results for flows with beds show that the fluid flow exhibits secondary vortices and an increase in the mean streamwise vorticity caused by corners in the cross-sectional plane of the pipes, with their intensity near the upper curved wall increasing with H_b. However, the upper vortices remain relative weak compared to those in lower regions of the pipes. The increase in mean streamwise vorticity in the half pipe is larger than that in the three-quarter pipe near the upper curved wall, while similar near the flat pipe floor due to the resistance of the curved wall to secondary motions. The movement of the particles in the cross-sectional plane is consistent with that of the secondary flows, but with slightly lower velocities. In regions near the wall away from the pipe corners, particle concentration in the half pipe is lower than in the three-quarter pipe, most likely due to its thinner boundary layer. This is reversed for concentration maxima near the pipe corners because of the magnitude of the secondary flows. Finally, the secondary flow changes the deposition or resuspension rate of the particles, particularly near the pipe corners, but these are always less than equivalent rates in the full pipe flow, which is likely caused by the magnitude of the wall unit.

1. Introduction

Turbulent flows through pipes are ubiquitous in engineering applications such as water supply, ventilation and the transportation of oil and gas. In all these applications, solid materials are frequently carried by the fluid medium to transport them to a desired location. The presence of a particulate phase considerably complicates the pipe's flow dynamics. For example, high concentrations of hydrates in oil pipelines may be deposited at the bottom of a horizontal pipeline due to the gravitational force. This in turn affects extraction efficiency and pipeline life (Wang et al., 2022, Zhang et al., 2022). In gas pipelines, sulfide in the gas reacts easily with the pipeline metal and produces impurities. These impurities are removed from the wall by erosion by the flow of natural gas and can again deposit at the bottom of a horizontal pipeline (Sherik et al., 2008). Material deposition in turbulent pipe flows is not only of importance in industrial applications, since such deposits will impact the flow field and particle transport potentially resulting in flow restrictions or even pipe blockages, but is also of scientific interest because of the interactions between the flow field and the particles due to the existence of secondary flows in the cross-sectional plane of the

* Corresponding author.
E-mail address: l.f.mortimer@leeds.ac.uk (L.F. Mortimer).

https://doi.org/10.1016/j.ijmultiphaseflow.2023.104625
Received 31 May 2023; Received in revised form 19 August 2023; Accepted 27 September 2023
Available online 28 September 2023

pipe. Despite interest in this field, studies concerning the relationship between material deposition and its impact on the flow field and particle transport in pipes is lacking, with the particle sizes involved in most experimental studies generally (Arolla and Desjardins, 2015) being of order 100 μm which consequently take significant periods of time to deposit and affect the turbulent flow.

In this work we circumvent this issue by using direct numerical simulation-based predictions of an infinite length of horizontal pipe, with particle dispersion accommodated using Lagrangian particle tracking. Deposited particle beds are handled in a simplistic way as flat solid surfaces (Liu et al., 2021a, 2021b) at the bottom of the pipe. Nevertheless, plane flat beds that do not vary with time are one form of bed type found in depositing flows (Rice et al., 2017). Additionally, particle deposition, bed formation and evolution are complex processes that would entail high computational costs to predict as the use of boundary resolving approaches would be required. In this work, therefore, and given that flat beds are one category of bedform, the simplified approach adopted, although idealised, allows the present study to focus on the impact of the secondary flows, caused by the simulated particle beds, on particle behaviour.

Since the present study involves particles interacting with the turbulence field which arises due to a non-trivial geometry, the characteristics of the secondary flows generated in a range of geometries including pipes as well as square, triangular and elliptical ducts are of relevance. In 2011, Larsson et al. (2011) used a horizontal semicircular duct as an experimental pipe (with the height of the pipe smaller than its radius) and measured the turbulence field within it using laser-Doppler velocimetry. Under the condition of a bulk Reynolds number of 80,000, they observed secondary flows in the flow field and successfully predicted this phenomenon using a Reynolds-averaged Navier-Stokes approach closed using a Reynolds stress turbulence model. In addition, a large eddy simulation-based study was also carried out in the same pipe with a flat bed, and the resulting particle distribution analysed (Liu et al., 2021). It was found that the streamwise vortices near the curved boundary are significantly different from those near the flat floor, which had a unique effect on the motion of the particles. Due to a lack of more detailed experimental data and the difficulty in predicting the influence of the large eddy simulation filtering employed on the secondary flows and particle behaviour, more accurate studies of the turbulence field and particle motion in similar pipes with simulated beds are warranted. In addition, laminar flow in a semicircular duct has also been simulated (El Hasadi et al., 2007). Under thermal boundary conditions, secondary flows were found to form due to buoyancy effects, but the formation mechanism of these secondary flows is different from when they form due to the confining geometry of the pipe or duct. Without the effects of heat transfer, no secondary flows were observed in similar laminar flows in a semicircular duct (Alassar, 2014).

Secondary flows in turbulence, of Prandtl's second kind, give rise to an average transverse flow of fluid superimposed on the streamwise flow due to the anisotropy of the turbulence, with a magnitude in the range of 1%-3% of the mean streamwise velocity (Bradshaw, 1987, Nikuradse, 1930, Prandtl, 1926, Brundrett and Baines, 1964, Gavrilakis, 1992, Madabhushi and Vanka, 1991, Pirozzoli et al., 2018). Different from secondary flows of the first kind, which occur within curved flows under the action of centrifugal effects and where transverse velocities up to 40% of the mean streamwise velocity can occur (Flack and Brun, 2003, Liou et al., 2003, Noorani et al., 2016), flows of the second kind can be generated in straight pipes and have less influence on the streamwise flow (Bradshaw, 1987, Nikuradse, 1930, Prandtl, 1926, Brundrett and Baines, 1964, Gavrilakis, 1992, Madabhushi and Vanka, 1991, Pirozzoli et al., 2018). For example, in a turbulent square duct flow, the fluid flows from the centre of the duct to its corners, then returning to the centre of the flow along the walls (Bradshaw, 1987, Nikuradse, 1930, Prandtl, 1926, Brundrett and Baines, 1964, Gavrilakis, 1992, Madabhushi and Vanka, 1991, Pirozzoli et al., 2018). Due to the symmetry of the duct, there are eight secondary vortices in its cross-section which transport momentum and change the distribution of the mean streamwise velocity and other turbulence statistics (Bradshaw, 1987, Nikuradse, 1930, Prandtl, 1926, Brundrett and Baines, 1964, Gavrilakis, 1992, Madabhushi and Vanka, 1991, Pirozzoli et al., 2018). In a rectangular duct, the vortex near the shorter side is smaller, but the overall pattern of the secondary flows is close to that in a square duct (Vinuesa et al., 2014, 2016). Secondary flows can also be generated in a right-triangular duct (Hurst and Rapley, 1991). However, due to the asymmetry of the duct, the secondary vortices near the corners are of different sizes and have different characteristics. In hexagonal tubes the secondary flows exhibit similar characteristics (Marin et al., 2016). Thus, although the corners of the tube reach 120°, the fluid still moves from the centre of the tube to the corners along the corner bisector, with vortex pairs associated with each corner of the tube (Marin et al., 2016). The secondary flows in elliptical ducts are unusual (Nikitin and Yakhot, 2005) because the ellipse clearly does not have corners. However, the boundary curvature at both ends of the long axis of the ellipse is large, with a significantly lower boundary curvature at either end of the short axis. The boundaries at either end of the major axis therefore act like corners in a square duct, with two counter-rotating vortices formed around the major axis, with the fluid flowing along that axis from the centre of the duct and returning along the curved walls (Nikitin and Yakhot, 2005).

Due to the influence of the secondary flows, the behavior of particles in the pipe will also change. For example, in square duct turbulent flows, the secondary vortices cause particles to move within a single vortex at longer time scales (Sharma and Phares, 2006). Under the action of gravity, large heavy particles may modify the characteristics of the secondary flow, resulting in asymmetry in the vortices (Lin et al., 2017). Even when the particles have the same density as the fluid, their presence enhances and changes the structure of the secondary flows (Lin et al., 2017). In addition, the lift force on the particles also changes their behaviour, although this force is mainly derived from the large gradient in the streamwise mean velocity near the walls (Winkler and Rani, 2009). The influence of the secondary flows on the particle concentration distribution is also very significant. In a square duct flow, for example, the concentration of particles is greatest in the viscous sub-layer at the centre of the walls which is caused by fluid movement from the corners back to the duct centre (Yao and Fairweather, 2010, 2012). In contrast, in rectangular ducts, the location of the highest concentration of particles is nearer the corners due to the different characteristics of the secondary flows (Noorani et al., 2016).

The main objective of the work described is to quantitatively characterise the turbulent flow and particle distribution in two pipes with a flat bed using direct numerical simulation and Lagrangian particle tracking methods. The geometric models considered include a full pipe, three-quarter pipe and a half pipe. The mass flow rate through the different pipes was kept the same to simulate practical situations where the flow rate would be maintained by a pump. Therefore, the equivalent diameter-based Reynolds numbers for the full pipe, three-quarter and half pipe are 5300, 5909 and 7494 (Re_τ = 360, 401 and 509 using the shear stress calculated at the midpoint of the pipe floor for the cases with beds), respectively. A detailed assessment of the most relevant turbulence features is reported, including mean flow and Reynolds stress tensor components. In all three pipes, the particle size and volume fraction are the same, but the Stokes number is not due to fluid timescale variations. For the particles, concentration, mean velocity, Voronoi diagrams, and deposition and resuspension rates are considered and analysed. The simulation is one-way coupled in order to focus the study on the influence of the secondary flows on the particles and eliminate the complexities introduced by other factors.

2. Methodology

2.1. Flow configurations

The flow geometries and coordinate system are shown in Fig. 1, with

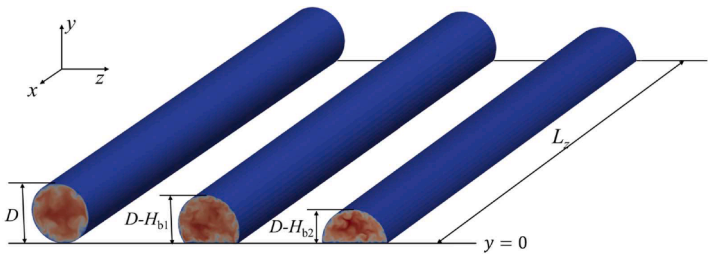

Fig. 1. Coordinate system and geometry of pipes with different beds, contours show instantaneous streamwise velocity. $H_{b1} = 0.25D$, $H_{b2} = 0.5D$, $L_x = 4\pi D$.

the colour representing the instantaneous streamwise velocity of the fluid. The diameter of the three pipes is D and the radius is R. For the three-quarter and half pipes, a bed of height H_{b1} and H_{b2}, respectively, exists at the bottom on the pipe, reducing their volume. A Cartesian coordinate system with x, y and z in the streamwise, vertical and spanwise directions, respectively, is used, with corresponding fluid velocities of u, v and w. The origin of the coordinate system is the lowest point of the full pipe, and the centre of the flat surface for the pipes with simulated beds. The length of the pipes is $L_x = 4\pi D$ which is sufficient to accommodate the largest turbulent coherent structures in the streamwise direction and meet the requirements of periodic boundary conditions (Robinson, 1991, Jimenez and Hoyas, 2008). No-slip boundary conditions are applied to the pipe wall and flat bed.

To be as consistent as possible between the flows, when the lower regions of the pipe are considered to be filled with sediment, a pump with a fixed volumetric flow rate is assumed to drive the flow. Therefore, the bulk velocity of the fluid flow in the half pipe is twice that in the full pipe, with the bulk velocity in the three-quarter pipe in-between the two. The pipe diameter D is used as the characteristic length for all three cases. The Reynolds number of the flow in the full, three-quarter and half pipes is 5300, 5909 and 7494, respectively, based on the equivalent pipe diameter and velocity scales.

2.2. Direct numerical simulation

The direct numerical simulation code, Nek5000[35], is used to calculate the three flows. The code is based on the spectral element method, and each computational domain is divided into hexahedral elements. Due to its high precision and high efficiency parallelisation characteristics, it is widely used to predict wall-bounded flows (Vinuesa et al., 2014, Noorani et al., 2016, Mortimer et al., 2019, El Khoury et al., 2013).

The numerical meshes used are shown in Fig. 2, where each geometry is divided into different elements and different structures. For the

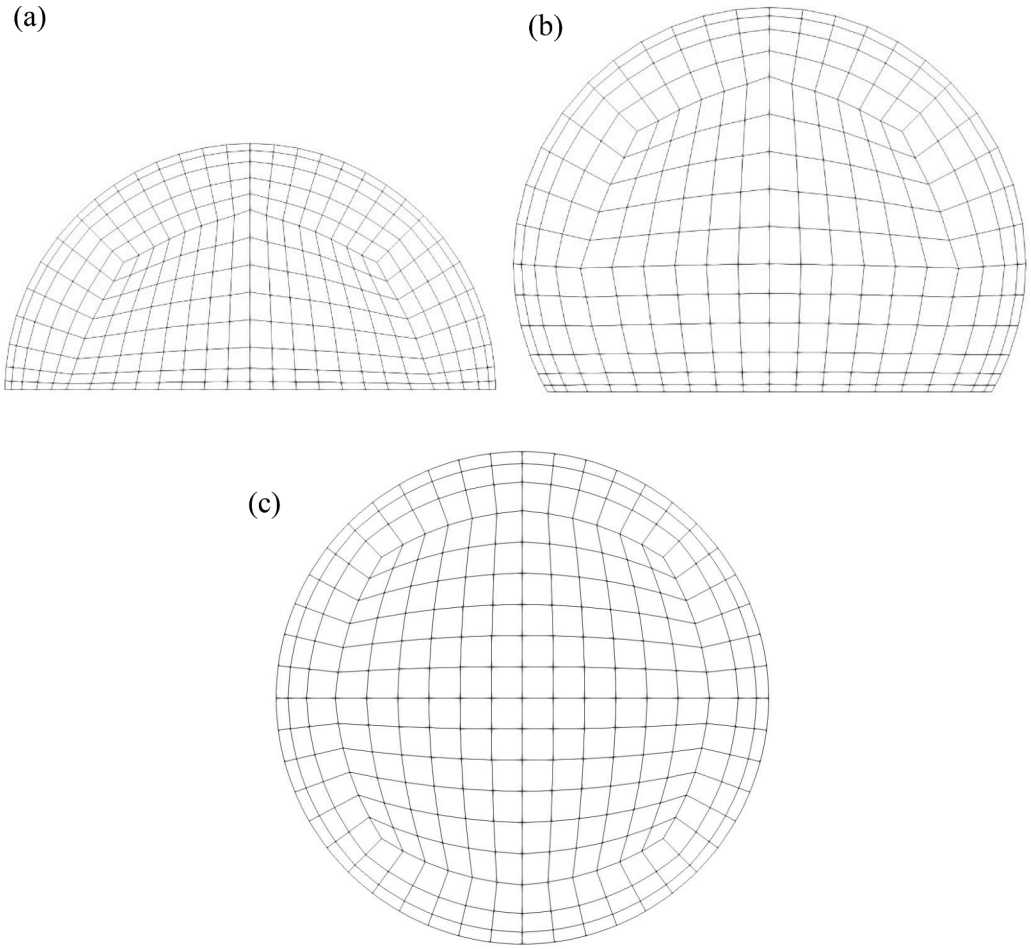

Fig. 2. Cross-stream spectral element mesh considered in each pipe, with a total of 288, 268, and 286 elements in the y-z plane for (a), (b) and (c), respectively.

full pipe, the continuous phase is discretised into 286 (cross-section) × 128 (streamwise) eighth-order spectral elements, while equivalent values for the three-quarter and half pipes are 268 × 128 and 288 × 128, respectively. Nodes in all meshes are uniformly distributed in the x direction. In the streamwise direction, the mesh spacing in wall units ranges from $\Delta x^+ =$ 10-30, while in the cross-section the range is 0.3–12. The time step (non-dimensionalised using the bulk flow timescale) is set constant at $\Delta t^* = 0.001$ which ensures that the Courant number is always less than 0.5. From here on, any variable labelled with an asterisk (*) will be used to denote a quantity non-dimensionalised by bulk properties, whereas a plus sign (+) denotes non-dimensionalisation by shear scales. In addition, a pressure gradient is applied in the x direction in order to drive the flow. The Navier-Stokes equations, which are non-dimensionalised using the pipe diameter and bulk velocity, may be stated in general non-dimensional form as:

$$\nabla\cdot\vec{u}^* = 0, \tag{1}$$

$$\frac{\partial\vec{u}^*}{\partial t} + \vec{u}^*\cdot\nabla\vec{u}^* = -\nabla p^* + \frac{1}{Re_b}\nabla\cdot\tau^* + \vec{f}^*, \tag{2}$$

where $\vec{u}^*$ is the fluid velocity, $\vec{p}^*$ is the fluid pressure, τ^* is the viscous stress tensor, and $\vec{f}^*$ is the additional applied pressure gradient term, ensuring that the mass flux of the flow remains constant. More details on the spectral element method and code may be found elsewhere (Vinuesa et al., 2014, Noorani et al., 2016, Fischer et al., 2008).

2.3. Lagrangian particle tracking

The Lagrangian particle tracking technique is used to predict particle motion (Mortimer et al., 2019). In fully developed turbulence, particles move along calculated trajectories. Particles are treated as point spheres, and the size of the particles is smaller than the minimum Kolmogorov length scale (Kuerten, 2016). The forces acting on the particles typically include the drag, lift, virtual mass, pressure gradient and Bassett history forces, together with gravity and buoyancy (Maxey and Riley, 1983). According to the work of Armenio and Fiorotto (Armenio and Fiorotto, 2001), when the density ratio range is $O(1)$, the pressure gradient force should be considered. In this work, the fluid is considered as water and the particle density ratio is 2.71, so the pressure gradient force cannot be ignored. The Bassett history force is not considered because the integration time used in this work is short and the particle size is small, which makes the Bassett history force much smaller than the drag force (Pan and Banerjee, 1996). In addition, particle interaction, gravity and buoyancy are not considered to focus the study more closely on the effect of the fluid flow on particle motion. Lift due to particle rotational dynamics is also ignored (Zeng et al., 2009). The particle volume fraction considered is 10^{-3}, but the high particle number chosen is to enable converged particle statistics upon analysis, rather than to predict a specific concentration of particles in the flow. That said, collisions between particles (Elghobashi, 1994) will be considered in future studies. All particles are treated as rigid spheres of the same size, and collisions between particles and walls are treated as fully elastic.

Based on the above assumptions, the dimensionless equation of motion for the particle velocity, solved in conjunction with that for the particle position, can be given as follows:

$$\frac{d\vec{u}^*_p}{dt^*} = \frac{3C_D|\vec{u}^*_s|}{4d^*_p\rho^*_p}\vec{u}^*_s + \frac{3C_L}{4\rho^*_p}(\vec{u}^*_s\times\vec{\omega}^*) + \frac{C_{am}}{\rho^*_p}\left(\frac{d\vec{u}^*}{dt^*} - \frac{d\vec{u}^*_p}{dt^*}\right) + \frac{1}{\rho^*_p}\frac{d\vec{u}^*}{dt^*} \tag{3}$$

On the right side of this equation are the drag force, shear-induced lift force, added-mass force and pressure gradient force terms. $\vec{u}^*_p$ is the particle velocity, $\vec{u}^*_s = \vec{u}^* - \vec{u}^*_p$ is the slip velocity, with the fluid velocity at the position of the particle obtained through spectral interpolation, and d^*_p is the particle diameter. The particle to fluid density ratio is $\rho^*_p = \rho_p/\rho_f$, where ρ_p is the particle density. $\vec{\omega}^* = \nabla\times\vec{u}^*$ is the vorticity of fluid. C_{am} is the added-mass force coefficient, which is 0.5 for a sphere. C_D and C_L are the Stokes drag and slip lift coefficients (Zeng et al., 2009, Schiller and Naumann, 1933), which vary with the gap distance between the particle and the wall, δ:

$$\begin{cases} C_D = 24/Re_p, & Re_p \le 0.5 \\ C_D = 24/Re_p\cdot\left(1+0.15Re_p^{0.678}\right), & 0.5 < Re_p < 1000 \\ C_D = 0.44, & Re_p \ge 1000 \end{cases} \tag{4}$$

with

$$Re_p = Re_b d_p\left|\vec{u}^*_s\right| \tag{5}$$

In addition,

$$C_L = C_{ls}\exp\left(-0.5\delta(Re_G/250)^{4/3}\right)\times\left(\exp\left(\alpha(Re_G)\delta^{\beta(Re_G)}\right) - \lambda(\delta, Re_G)\right) \tag{6}$$

$$\begin{cases} C_{ls} & = 3.663/\left(Re_G^2+0.1173\right)^{0.22} \\ \alpha(Re_G) & = -\exp(-0.3+0.0025Re_G) \\ \beta(Re_G) & = 0.8+0.01Re_G \\ \lambda(\delta, Re_G) & = (1-\exp(-\delta))(Re_G/250)^{5/2} \end{cases} \tag{7}$$

with

$$Re_G = Re_b {d^*}_p 2|\vec{\omega}^*| \tag{8}$$

The fourth order Runge-Kutta method is used to integrate the particle equations of motion. Initially, particles are randomly injected into the pipe domain, and the initial velocity of the particles is set to be the same as the local fluid velocity. The particle solution time step is the same as the flow time step, which is much smaller than the particle relaxation time. Therefore, the trajectories of particles are fully resolved. Similarly, at the inlet and outlet boundaries of the pipes, the particles are treated as periodic, that is, the particles flowing out of the pipe are reintroduced into the inlet. The particle-fluid density ratio is 2.71, with the continuous phase considered as water and the particulate phase as calcite. There are different quantities of particles in the different pipe geometries to ensure the same particle volume fraction in all three cases, which is 150,000, 120,000 and 75,000 for the full, three-quarter and half pipes, respectively. The dimensionless relaxation time of the particles and Stokes number can be used to characterise the importance of particle mass. The Stokes numbers based on the viscosity scale (using the shear Reynolds number calculated at the centre of the pipe floor for cases with beds) and integral scale (using the bulk Reynolds number) are as follows:

$$St^+ = Re_\tau^2\frac{d_p^{*2}\rho_p^*}{18} \tag{9}$$

$$St_b = Re_b\frac{d_p^{*2}\rho_p^*}{18} \tag{10}$$

For the particle properties used in this study, the Stokes numbers based on the friction wall scales are 0.5, 1.2 and 1.9 for the full, three-quarter and half-pipes respectively, which correspond to Stokes numbers based on the Kolmogorov timescales, τ_η, of 0.017, 0.03 and 0.06 respectively.

3. Results and discussion

In this section, the single-phase flow and particle distribution in pipes with different bed thicknesses are analysed. Before this, the flow field in the full pipe is fully validated to ensure the reliability of the

calculation method. We will then focus on the turbulent secondary flow in the pipes and the resulting statistical characteristics of the particles.

3.1. Multiphase flow validation

To illustrate the accuracy of the current simulation approaches, the flow field in a full pipe with $Re_\tau = 277$ and 360 is compared with the results obtained by Vreman (2007) and Rani et al. (2004). The variables are averaged after the turbulent flow has fully developed, ensured by monitoring the statistical profiles at regular intervals until they were exhibiting negligible changes with time. Since the full pipe flow is axisymmetric, the average of any variable does not take into account either the position along the pipe or the angle in the cross-section, but only distance from the wall. It is worth noting that this is different for the three-quarter and the half pipe due to the incomplete symmetry of their cross-sections. As shown in Fig. 3, for one-way coupling, both the mean velocity, the root mean square of velocity fluctuations and the major shear stress are in good agreement with predictions of Vreman (Vreman, 2007) and Rani et al (Rani et al., 2004). Minor discrepancies are observed when comparing the $Re_\tau = 360$ case, attributed to the differences in numerical method, as well as reduced spatial and temporal resolutions employed in the comparison study.

3.2. Continuous phase flow field

For the fluid phase, a completely uniform velocity superimposed with sufficiently chaotic sinusoidal fluctuations is taken as the initial state of flow field calculation, which then ensures that the flow reaches a fully developed state as soon as possible. The flow field is confirmed to be fully developed by monitoring the average velocity and the turbulence statistics. Fluid statistics are collected over 1500 integration time units. In addition to time averaging, since there is spatial symmetry in the streamwise (x) direction, as well as mirror symmetry about the $y-z$ plane, the statistics were spatially averaged in the streamwise direction, and then across the left and right half planes of the flows with simulated beds.

To ensure the mesh was sufficient to capture flow resolution below

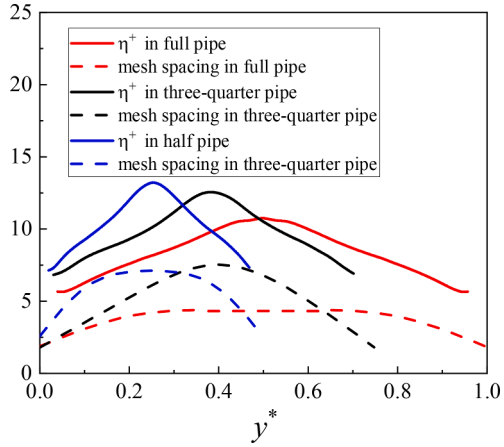

Fig. 4. Kolmogorov length scales and mesh spacing in the cross-section along the center line of different pipe, normalized by wall unit.

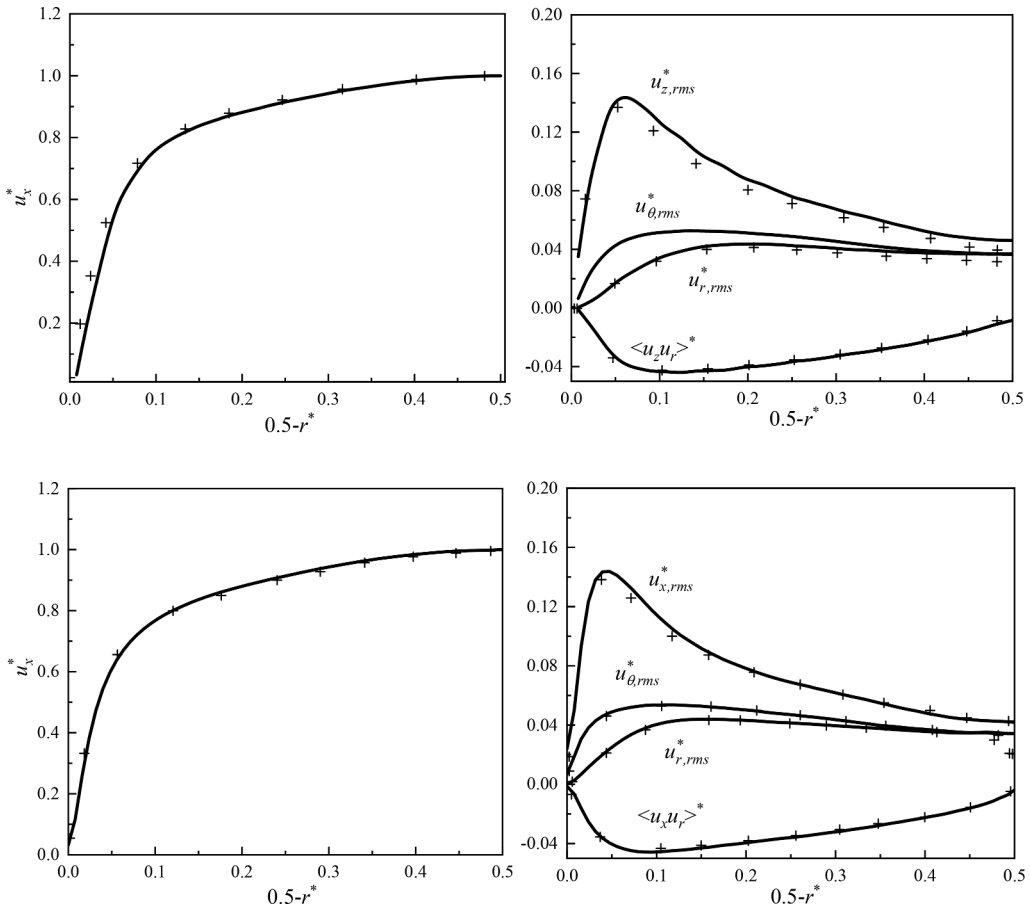

Fig. 3. Predictions of streamwise mean velocity (left), root-mean-square of streamwise, radial and circumferential velocity fluctuations, and shear stress (right). Comparison with Vreman (2007) at $Re_\tau = 277$ (top) and Rani et al. (2004) at $Re_\tau = 360$ (bottom). Solid lines: present work; Symbols: predictions from Vreman and Rani et al.

the Kolmogorov length scale, η^+ was measured across the vertical direction and is compared to the local mean cell spacing in Fig. 4. In all cases, the mean mesh spacing is approximately half that of the Kolmogorov length scale, guaranteeing that the important smallest-scale flow features are captured, and ensuring the simulated particle dynamics respond to an accurate flow field. To further confirm DNS is being performed, the energy spectral densities of the streamwise velocity fluctuations in each case (and at various distances from the wall) are provided in Fig. 5. In all cases, the decay is demonstrated to be consistent with the -5/3 power law.

Fig. 6 shows contours of the mean cross-stream velocity and the mean x-velocity magnitude, as well as the secondary motion vectors and streamlines, which are normalised using the bulk velocity.

The secondary flows in the half pipe are shown in Fig. 6(a). The fluid flows from the centre of the pipe to the corner and then back to the centre along the pipe wall, which is consistent with other reported turbulent secondary flows (Larsson et al., 2011, Vinuesa et al., 2014, Marin et al., 2016, Huser and Biringen, 1993). Interestingly, the size of the secondary flow near the bed is much larger than that near the upper wall, above the corner bisector, which is at variance with other reported results. In addition, the shape of the secondary flow near the upper wall is also significantly different from that near the floor. This is due to the limiting effect of the curved wall on circumferential velocity fluctuations and the consequent extension of the secondary vortices near that wall.

It is known that turbulent secondary flows result from the interaction of turbulent coherent structures near two adjacent walls (Marin et al., 2016, Huser and Biringen, 1993). Near the wall, there are ejection and sweep events, collectively referred to as burst events. In the boundary layer, ejection and sweep events are balanced due to continuity considerations, with ejections in the wall normal direction, and sweep events tangential to the wall. Therefore, the direction of the burst events is not the same for the two different wall orientations. If two walls meet and form a corner, the burst events must interact with each other. In the corner, after a burst event occurs, momentum is transported from the flat boundary to the outer layer because the direction of the ejection event is not blocked, and the fluid moves along the wall away from the corner. At the same time, due to the presence of the adjacent wall, sweep events cannot occur normally. This creates an area of low pressure at a corner, causing fluid to flow from the centre to the corners.

For pipes with a simulated bed, differences from previous findings occur due to the shape of the adjacent pipe walls. The upper wall is an inward curved arc, while the bed is a flat surface with zero curvature. In full pipes, burst events occurring near walls have been found to be different from those at flat walls, and inwardly curved walls restrict fluid movement in the circumferential direction, thus creating restrictions on sweep events (Elghobashi, 1994). The greater the curvature, the greater

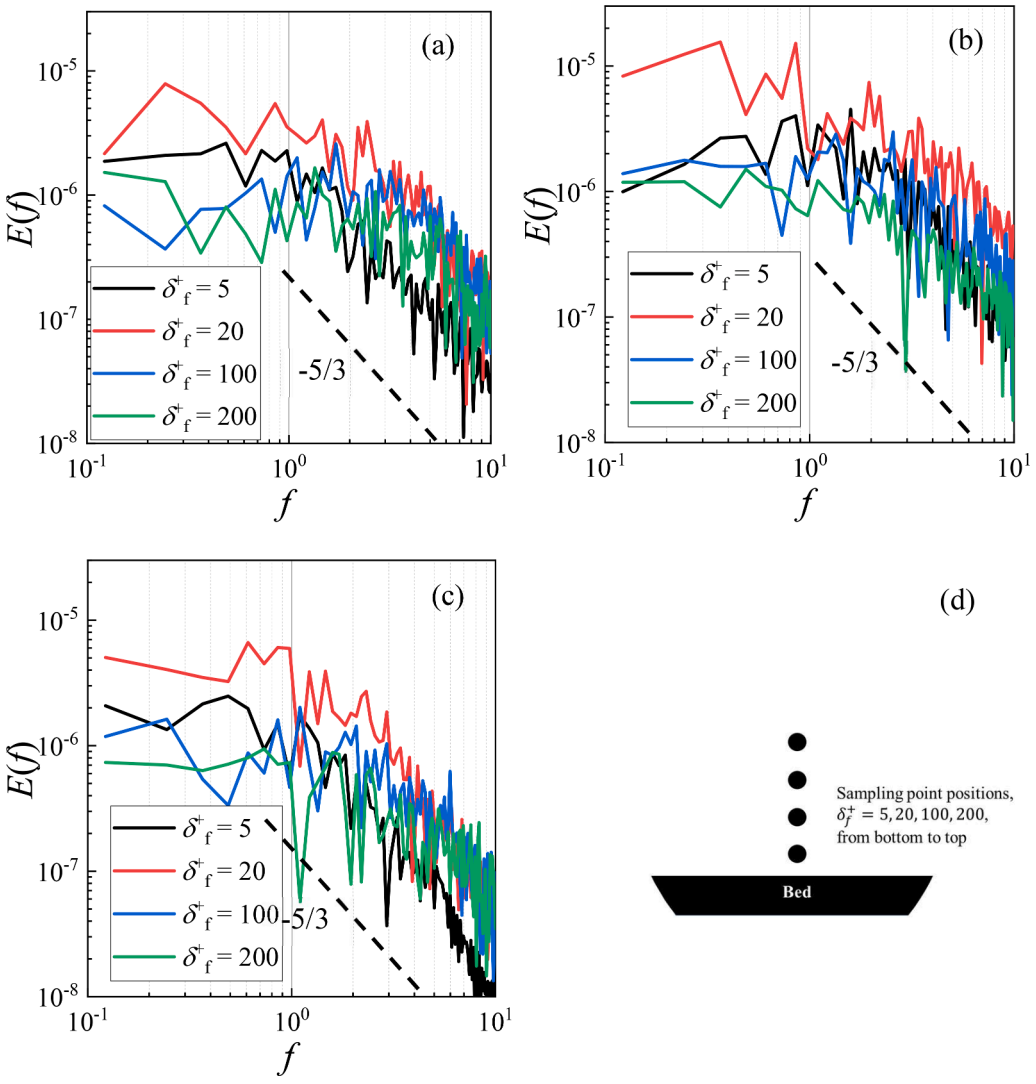

Fig. 5. The energy spectral density ($E(f)$) with frequency f, normalized by Du_b and u_b/D, of the streamwise velocity fluctuation at points at different distances from the bed of (a) half pipe, (b) three-quarter pipe and (c) full pipe. (d) The sampling point positions. Dashed lines are reference to the slope of -5/3.

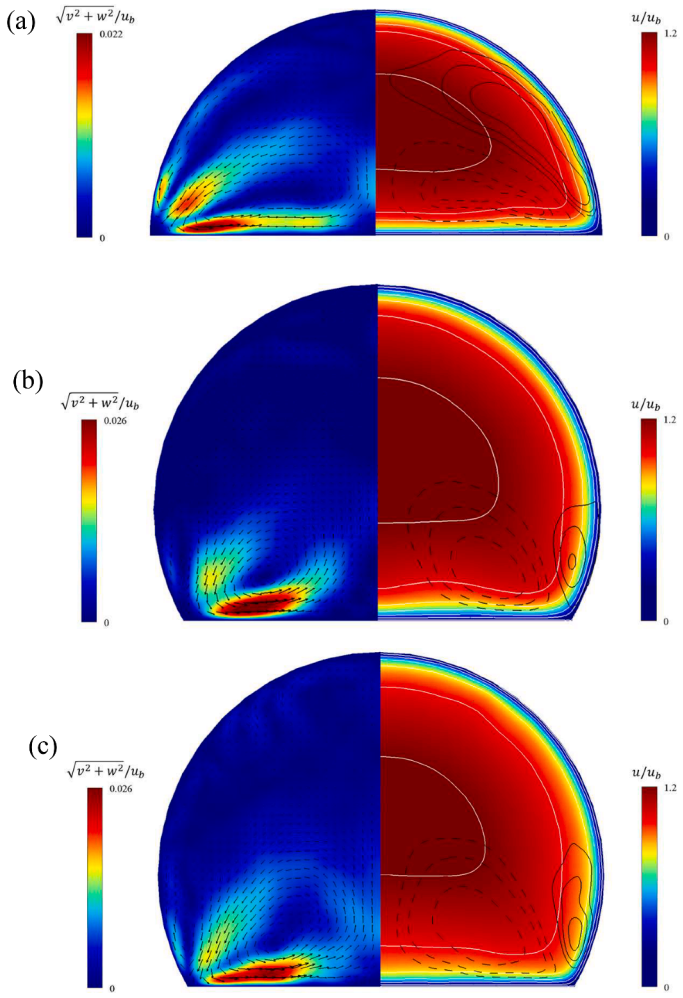

Fig. 6. Contours of the magnitude of the mean cross-stream velocity of the fluid flow (ms^{-1}) with superimposed vectors (left), and of the mean streamwise velocity together with isocontours of the cross-flow stream function (right) where dashed lines represent negative values of ψ. The velocity and length scales used are the bulk velocity u_b and the pipe diameter D, respectively. (a) half pipe (Re = 7,494), (b) three-quarter pipe (Re = 5,909), and (c) three-quarter pipe (Re = 7,494).

the limitation. This effect causes the fluid to flow along the wall to the area of lower curvature in elliptic pipes, thus inducing the generation of secondary flows (Nikitin and Yakhot, 2005). In a pipe with a simulated bed, the curvature of the upper wall obviously also limits the circumferential motion of the fluid. Therefore, the secondary flow near the upper wall is weaker.

Fig. 6(b) shows equivalent results for a bed height $H_b = 0.25D$ (three-quarter pipe). Compared with the half pipe, the secondary flow pattern has changed significantly. Therefore, although the fluid similarly flows from the centre to the corner and then returns along the wall to the centre of the pipe, the streamwise vortices near the upper wall become smaller and less intense. In contrast, the intensity of the secondary flow near the bed is not only much larger than that near the upper wall, but is also greater than that near the bed of the half pipe. In addition, at the top of the pipe, away from the corners, induced small vortices are generated that cannot be eliminated by larger averaging timescales.

Obviously, the differences between these secondary flows in the two pipes can be attributed to differences in geometry. Compared with the half pipe, the three-quarter pipe has a larger cross-section area, longer curved wall and shorter bed. In addition, the two walls meet to form a larger angle. Because of its larger cross-section area and same mass flow rate, the bulk velocity in the three-quarter pipe is also smaller than that in the half pipe. These factors work together to cause changes in the secondary flow and the effect of these factors is now discussed.

First, a larger angle where the curved and flat walls meet attenuates the interaction of turbulence near the adjacent walls. When this angle is increased to 180°, it is clear that this interaction does not exist. Therefore, the smaller the angle, the more the corner can promote the generation of secondary flows. In the three-quarter pipe, the increase in this angle weakens the intensity of the secondary flow near the upper wall. Similarly, this effect is also of importance to the secondary flow near the bed, but the difference is that the intensity of the secondary flow here is increased. This is because the secondary flow near the bed is not limited by the inward curvature of the upper wall, and the increase in the angle has a smaller effect on this secondary flow. In addition, due to continuity considerations, most of fluid flowing from the centre to the corner can only return along the bed, instead of via upper wall, to the centre of the pipe. Because the pipe cross-section is larger and the upper wall is longer, the upper regions of the three-quarter pipe are less affected by the corner turbulence dynamics. This results in a few small vortices towards the top of the pipe induced by secondary flow at the corners. Finally, in order to demonstrate the influence of Re on the secondary flows, a flow in the three-quarter pipe with the same Reynolds number as that in the half pipe (Re = 7,494) is simulated, with the results shown in Fig. 6(c). Obviously, the pattern of the secondary flow changes slightly at higher Reynolds number. Compared with Fig. 6(b), the secondary flow becomes larger near the side wall and the streamlines extend further away from the corner. At the same time, the maximum mean cross-stream velocity becomes smaller near the floor. In addition, near the vertical plane dissecting the pipe, the secondary flow is stronger. Because of the change in the secondary flow pattern, the contours of the streamwise mean velocity also change. The secondary flow near the floor no longer curves upwards from approximately a third of the bed length from the corner, but only towards the centre of the pipe (Fig. 6(c)). It is worth noting that, with the increase in Reynolds number, the streamwise mean velocity is more evenly distributed in the pipe, so the position of the isolines also changes, though qualitatively, the major flow features demonstrate significant differences with changes in geometry, rather than Reynolds number, therefore further analysis relates predominantly to comparing results obtained with the three bed heights.

In order to explain the effect of Reynolds number on the mean secondary flow pattern, the characteristics of turbulent secondary flows in square ducts are noted (Pinelli et al., 2010). When the Reynolds number is in the range of 2,000-3,500, the eddy and streamwise vorticity centres in a square duct gradually approach the wall with increasing Reynolds number, and the streamlines are closer to the walls. This phenomenon is related to the preferred position of coherent structure. In square ducts, when the Reynolds number increases, the preferred position of the high- and low-speed streaks which occur in the near-wall region of turbulent boundary layers is closer to the corners, with a higher probability of occurrence than near the centre of the walls where their probability of occurrence becomes more uniform as the Reynolds number increases (Pinelli et al., 2010). It is likely that smaller transient vortex structures and more chaotic momentum exchange at higher Reynolds numbers lead to this result. For a wall of infinite length, the distribution of these streaks is uniform as the fluid flows along the wall. Therefore, the change in distribution of the high- and low-speed streaks is due to the influence of the adjacent wall, and particularly due the influence of coherent structures in the turbulent flow of the boundary layer. When the Reynolds number increases, the boundary layer becomes thinner under the influence of smaller vortex structures and more chaotic momentum exchange, and the influence of the coherent structures in the flow is closer to the adjacent wall and the corner. Therefore, as the Reynolds number increases, the secondary flow away from the corner is less affected by the corner and more likely to flow along the wall. This is likely why the secondary flow adheres more to the wall at high Reynolds numbers.

For secondary flows near curved walls, although the motion of the

fluid is less affected by the corner at higher Reynolds number, the curved wall makes the secondary flows deflect from the wall as they flow along it. It is noted that at a Reynolds number of 40,000, the form of secondary flows predicted by large eddy simulation is significantly different from that found in the present work, with the vortex near the upper wall being significantly larger and stronger (Liu et al., 2021a, 2021b). This is due to the fact that fluids at high Reynolds numbers are able to move along the wall under the influence of inertia.

The distribution and intensity of the shear components of the Reynolds stress tensor for each case are presented in Fig. 7. In all cases, the high shear-stress regions present in the corners of the half-pipe are strengthened when compared to the three-quarter pipe, with the presence of the outward-facing wall permitting the formation of the turbulent secondary flows identified in Fig. 6. The $\overline{u'w'}$ component demonstrates more complex behaviour above the base of the pipe, with the direction reversing multiple times between either corner, likely to impact resuspension and deposition particle dynamics in that region.

Of more interest to the impact on particle dynamics is the gradient of the Reynolds stress tensor components, which impacts particle migration processes such as turbophoresis. Fig. 8 depicts contour plots of the Reynolds stress tensor components' gradients in the streamwise and vertical directions. In comparison with Fig. 7, it becomes apparent that the gradients of the Reynolds stress components on the cross-section exhibit a general correspondence with these components themselves. For instance, at upper left and upper right of the pipe cross-section, where *vw* exhibits its maximum value, a similar observation holds true for the gradients at that location. Similarly, the Reynolds stress components *uw* and *uv* exhibit maximal values on the left and right sides and upper and lower sides, respectively; correspondingly, their respective gradients along the *z*-direction and *y*-direction also display significant magnitudes here, despite these gradients being negative. This alignment is consistent with intuitive expectations, as these Reynolds stress components are intimately linked to the nearby wall. In proximity to the wall, turbulence invariably demonstrates pronounced anisotropy, wherein the magnitudes of fluctuations in various directions are distinctly influenced by the wall. Most intuitively, at the position nearest the center of the bed of the pipe, if there is positive fluctuation in the streamwise direction at a local region, due to the fluid's continuity, surrounding fluid will replenish this region within the cross-section. However, for fluid on the left and right sides, due to the pipe's symmetry, the probabilities of replenishment are equivalent, resulting in less correlation between streamwise and spanwise velocity fluctuations at that location. Conversely, in the vertical direction, only fluid above the bed of the pipe can replenish this region, as there is no fluid below it, leading to a correlation between vertical and streamwise velocity fluctuations. It is precisely due to this that the maxima of Reynolds stress components are intrinsically tied to the presence of the wall, and their gradients naturally exhibit maxima in the vicinity of the wall. Further from the wall, this mechanism generating Reynolds stress components diminishes, rapidly reducing the gradients of Reynolds stress components to nearly zero. Naturally, for Reynolds stress itself, the influence of the wall seems to extend over a more substantial range. Reynolds stress in proximity to the wall is elevated to higher levels due to wall effects; owing to the continuity of the fluid, stress cannot abruptly vanish and

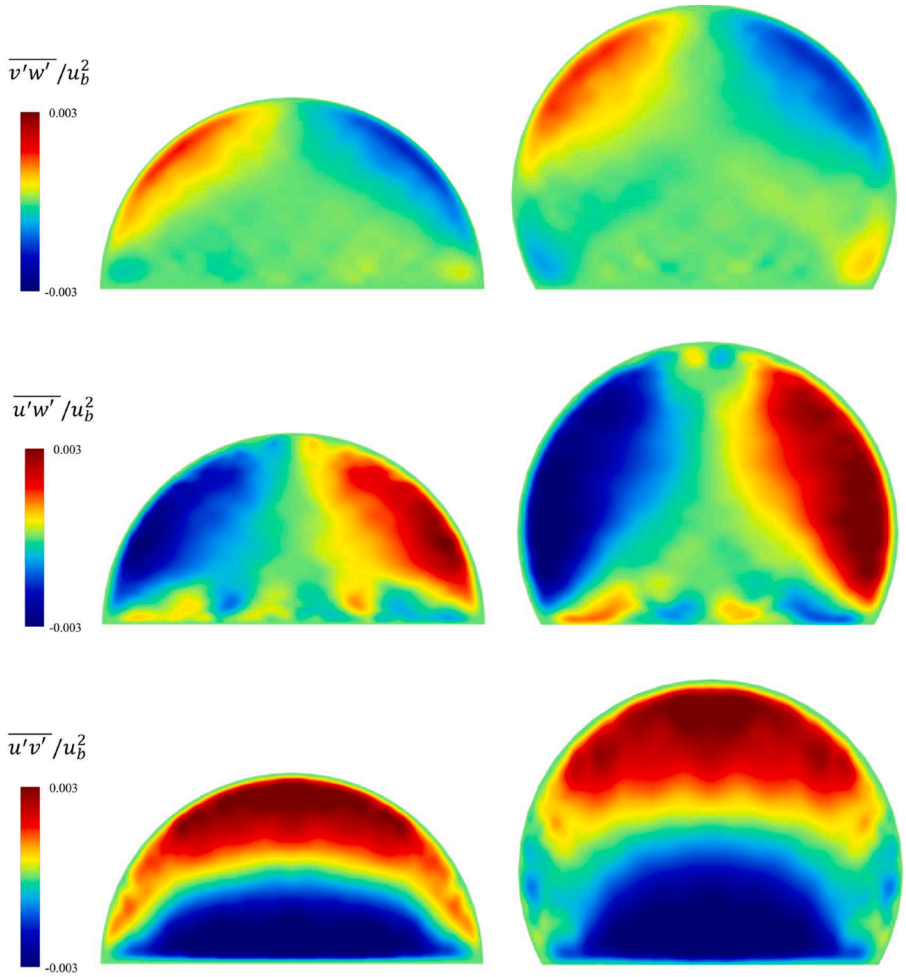

Fig. 7. Shear components of the Reynolds stress tensor non-dimensionalised by the square of the bulk velocity for the half-pipe (left) and three-quarter pipe (right). Top: $\overline{v'w'}$, middle: $\overline{u'w'}$ and lower: $\overline{u'v'}$.

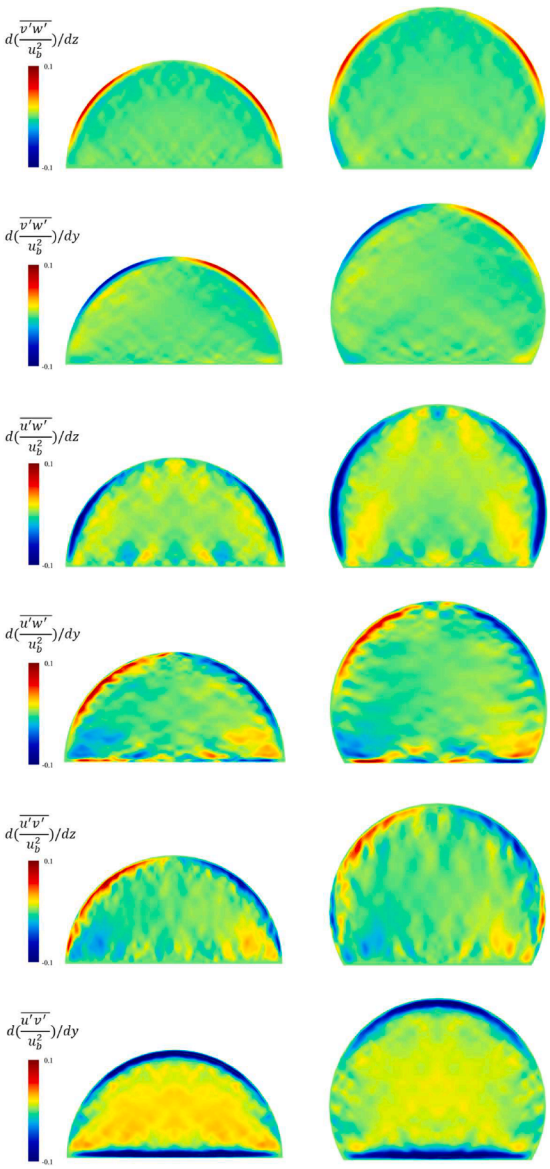

Fig. 8. Gradients of the Reynolds stress tensor components non-dimensionalised by the square of the bulk velocity for the half-pipe (left) and three-quarter pipe (right).

instead gradually diminishes from the wall towards the center. Similarly, at a slight distance from the wall, the gradients of these stress components and their orientations oppose those near the wall. These observations highlight the role of the wall in promoting the increase of Reynolds stress components and the dissipation of Reynolds stress components at the pipe's center.

The gradients of *uw* in the y-direction and *uv* in the z-direction exhibit maxima near the curved wall of the pipe, attributable to variations in the wall's shape. According to the aforementioned analysis, there consistently exists pronounced correlation between wall-normal velocity fluctuations and streamwise velocity fluctuations in proximity to the wall. Alterations in the direction of the wall's normal result in the rotation of the Reynolds stress tensor. Therefore, in essence, these extrema merely signify the transformation of Reynolds stress and Reynolds stress gradients from polar coordinates to Cartesian coordinates. The occurrence of maxima for vw itself and the gradients of *vw* at upper left and upper right can also be attributed to the manifestation of correlation between radial and tangential velocity fluctuations and their correlation gradients in the Cartesian coordinate system.

Fig. 9 shows the turbulence kinetic energy (TKE) normalized by the bulk velocity for the two bed thicknesses. The maximum values of the turbulence kinetic energy are all close to the upper and lower walls of the pipes. In the corner regions, although there is a greater probability of high- and low-speed streaks, these locations have lower values. This suggests that the coherent structures represented by high- or low-speed streaks represent a more stable (rather than chaotic) velocity distribution. Lastly, the secondary flows also affect the distribution of turbulence kinetic energy, and this influence is much greater than that of the secondary flows on the mean streamwise velocity, an effect found in other turbulent secondary flows (Esmaily et al., 2020), since the energy contained within them is close to the scale of the velocity fluctuations, and far smaller than that of the large-scale motion. In Fig. 9(c), the TKE along the centerline of the full pipe, the three-quarter pipe and the half pipe is compared. Maximum values in the two pipes with simulated beds are close, and significantly larger than those in the full pipe. This indicates that the secondary flow from the corners not only affects the distribution of velocity fluctuations, but also increases their intensity.

3.3. Particulate phase flow field

After the average statistics of the flow field reach stability, that is, the flow field is fully developed, the particles are injected randomly into the pipe domain. As previously mentioned, regardless of the effect of the particles on the fluid, the interaction between particles and the influence of gravity, the present work used one-way coupling with the Lagrangian tracking approach to capture the movement of the particles and the influence of the secondary flows. This approach avoids the influence of other complicating factors in order to focus the study specifically on the effect of the secondary flows on particle behaviour. Whether the particles reach a stable state or not is determined by calculating the number of particles near the pipe wall. In the range of $\Delta^+ < 5$ (where Δ is the distance from any position to the nearby wall), the concentration of particles near the upper wall and the bed is calculated with time. Similarly, a particle laden flow with the same particle concentration in the full pipe is also calculated, and the results are shown in Fig. 10, where local values are normalized by the bulk concentration C_b. It can be observed that the particles near different surfaces always increase and then stabilize with time, no matter whether in the full, three-quarter or half pipe. This is the result of the turbophoretic effect, which has been reported by many researchers (Noorani et al., 2016, Esmaily et al., 2020). Interestingly, there is a significant difference in the time taken for the particle distribution to reach full development in the different pipes, with the near-wall particle concentration in the full and three-quarter pipes taking longer to reach stability than the half pipe.

This occurs because the turbulence kinetic energy in the half pipe near the upper wall is steepest (Fig. 9(c)), with fewer particles affected in the region of the peak kinetic energy. In addition, for the half pipe, the wall unit is smaller than in the other cases, hence the particle sampling area is smaller due to the larger bulk flow velocity. These are likely the reasons the particle concentration in this pipe stabilizes most rapidly.

For the three-quarter and half pipes, fluid and particle velocities are collected along horizontal lines at $y = 1H_{pipe}/5$, $2H_{pipe}/5$, $3H_{pipe}/5$, and $4H_{pipe}/5$ (where the pipe height $H_{pipe} = D\text{-}H_{b1}$), with the results shown in Fig. 11. The velocity distribution for the continuous phase corresponds to the velocity contours shown in Fig. 6. It is noticeable that the secondary flow velocity of both particles and the fluid always has larger values in the lower regions of both pipes. For the half pipe, the horizontal and vertical velocities of the particles and fluid have their maximum values near the side wall along the line $y = 1H_{pipe}/5$, with the vertical velocities at a maximum value at pipe centre. At $y = 2H_{pipe}/5$, the horizontal velocity has a maximum value at $z/R = 0.4$, and the vertical velocity now has a smaller maximum than at $y = 1H_{pipe}/5$. In the upper regions of the pipe, both particle and fluid velocities are close to zero. In the three-quarter pipe, the maximum horizontal velocity of the particles and fluid reaches 0.1 at $y = 2H_{pipe}/5$, and then the maximum

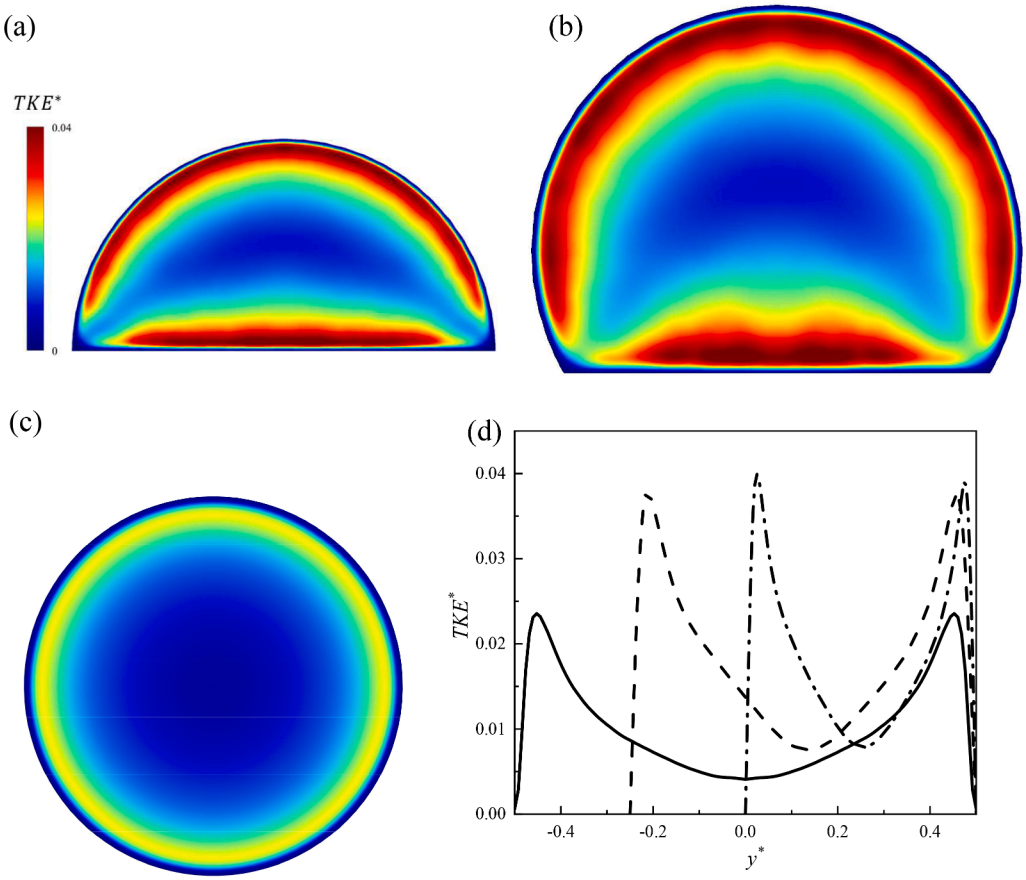

Fig. 9. Contours of turbulence kinetic energy of the fluid phase normalized by the bulk velocity $0.5u_b^2$ for (a) the half pipe, (b) the three-quarter pipe and (c) the full-pipe. (d) TKE along the center line of the full pipe (solid line), three-quarter pipe (dashed line) and half pipe (dash dot line).

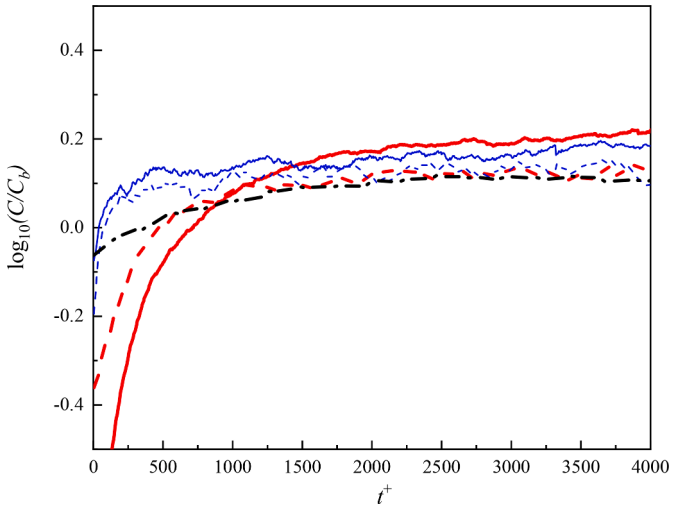

Fig. 10. Number of particles with distance less than $\Delta^+ = 5$ to the upper and lower boundaries of the pipes with beds, and the full pipe, as a function of time. Equal sized particles in all pipes with St = 0.5, 1.2 and 1.9 for particles in the full, three-quarter and half pipes. Black dash dot line: full pipe; Red solid line: upper wall of three-quarter pipe; Blue solid line: upper wall of half pipe; Red dashed line: floor of three-quarter pipe; Blue dashed line: floor of half pipe.

horizontal velocity gradually decreases with height, subsequently increasing again to 0.004 at y = $4H_{pipe}/5$. The vertical velocity of the particles and fluid again approaches 0 at $4H_{pipe}/5$. Clearly weak vortices in the upper regions of the three-quarter pipe do impact on particle behaviour, although not significantly.

Due to the small Stokes number of the particles they have little inertia, short relaxation times and are better able to follow the flow streamlines, so the slip velocity between the particles and the fluid is small. As shown in Fig. 11, the mean velocity of the particles is almost always less than that of the fluid. This is because the energy for moving the particles comes from the fluid. In a rectangular turbulent duct flow, it has been found that the velocity of the particles in the angular bisector region is significantly higher than that of the fluid, while the velocity of particles is lower than that of the fluid near the wall (Noorani et al., 2016). This variation with the present findings is explained by differences in particle inertia, with the density ratio adopted in this work of $O(1)$. Therefore, the inertia of the particles is the same order of magnitude as that of the local fluid, so the inertia of the particles does not significantly influence the slip velocity.

Fig. 12 shows the particle concentration near the wall. It has already been noted that the concentration of particles at this location is significantly greater than the mean concentration due to turbophoresis. This effect is evident in all the pipes considered, including the full pipe. However, the particle distribution near the wall is significantly different in the various pipes. For the half pipe, the concentration at the bed centre is only slightly higher than the mean volume fraction, and lower than the particle concentration near the wall of the full pipe. At $z/R = \pm 0.8$, this concentration increases to a maximum and then drops off near the pipe corners. For the three-quarter pipe, the particle concentration near the centre of the bed is similar in magnitude to that in the full pipe, increasing slightly to maximum values at $z/R = \pm 0.6$ and then decreasing again near the corners. For the upper wall of the three-quarter pipe, the particle concentration reaches its maximum value near $y = 0$ ($\theta \approx 0$ and π), and is higher than that near the wall of the full

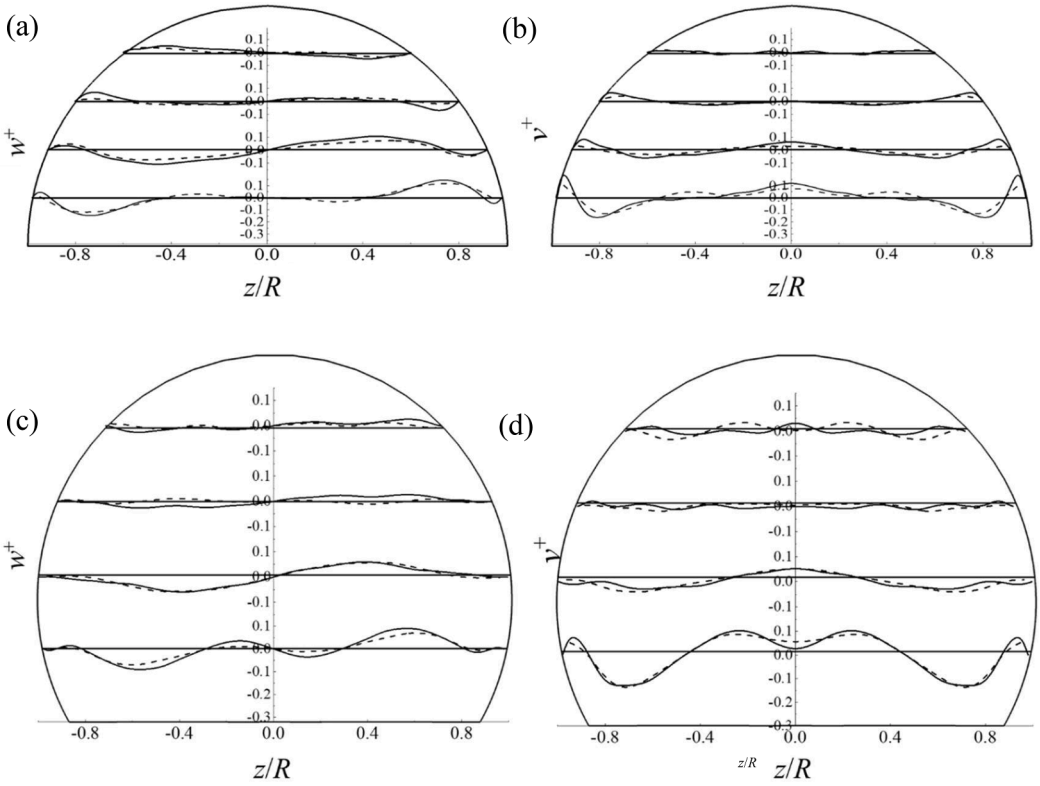

Fig. 11. Time-averaged cross-stream velocity of fluid (solid lines) and particles (dashed lines) along four lines whose positions are 1/5 to 4/5 times the pipe height. (a) and (c), velocity in spanwise direction; (b) and (d) velocity in vertical direction.

pipe except close to the corners. For the half pipe, although the qualitative trend of particle concentration is similar to that of the three-quarter pipe, its magnitude is very different. The maximum particle concentration near the corners is therefore higher than in the three-quarter pipe, although much lower at the top of the pipe and closer to that in the full pipe.

The particle distributions observed can be explained in terms of the turbulence kinetic energy distribution and the secondary flows. As shown in Fig. 9, the gradient of TKE near the wall in the half pipe is greater than that in the three-quarter pipe, that is, the flow disorder in the half pipe is greater and the boundary layer is thinner. Since the average particle concentration in the different pipes is the same, the thinner boundary layer means that the number of particles affected by turbophoresis is smaller. As a result, the particle concentration near the upper and lower walls, far from the corner of the three-quarter pipe, is higher than that at similar positions in the half pipe. It is worth noting that the TKE magnitude in the full pipe is always lower than that in the three-quarter pipe and there is no mean secondary flow in the full pipe which can promote the cross-stream movement of particles. Therefore, the particle concentration near the wall of the full pipe is lower than that near the upper wall of the three-quarter pipe, except at the corners of the latter.

Near the pipe corners, the secondary flows have a significant effect on the particle concentration. Particles are carried from the centre of the flow to the corners by the secondary flows, and continue to move along the wall on either side of the corner, causing the number of particles approaching the corners to increase. Small Stokes numbers cause the particles to follow the streamlines, however, and not fully reach the corners of the pipe, accounting for the minima in those regions. As the average velocity of the fluid in the half pipe is higher and the absolute intensity of the secondary flow is larger (Fig. 6), the secondary flow has a more obvious effect on the particles in this pipe, and the particle concentration maxima near the corners are higher than in the three-quarter pipe.

The particle concentration near the pipe walls is similarly affected by the turbulence and secondary flow intensities, and the concentration in the y direction at $z = 0$ may be considered in this regard. The large Re in the half pipe causes particles to move more vigorously and concentrate in the bulk flow region, while secondary flows back to the centre cause a smaller concentration of particles near the walls (red circles in Fig. 12 (f)). This also occurs in the three-quarter pipe, but the effect is less significant due to the lower Reynolds number and secondary flow intensity.

The instantaneous distribution of particles close to the pipe boundaries and within the flow is also worthy of consideration. Here, a Voronoi tessellation approach is applied. By dividing the flow region into cells based on the location of the nearest particle, the diagrams reveal spatial variations in particle distribution. The size and shape of Voronoi cells can offer information about flow dynamics, revealing regions of high and low particle concentration, as well as potential particle clustering or segregation areas. Near the curved wall and the simulated bed, and on a horizontal surface at the centre of the pipes, particles within $\Delta^+ = 10$ at $t^+ = 4000$ are sampled and their Voronoi diagrams are presented in Fig. 13, where the colour represents the area of cells normalized by D^2. Lower areas hence indicate more clustering. Because the mean particle concentration near the walls of the half pipe is lower than in the three-quarter pipe, away from the corners at least, the Voronoi cells at the near-wall sampling locations of the half pipe are larger. Interestingly, the regions of small cells also do not form a streaky structure and are not randomly clustered.

Comparing the dynamics of both the half-pipe and the three-quarter pipe, it would appear that longer structures are observed in the half pipe, with particles clustering in streamwise-orientated regions. Though these are present in the three-quarter pipe, they appear thinner and more isotropic in orientation. In previous studies of flows in square ducts with higher Stokes number particles, for $St^+ = 25$ particle concentration streaks are formed near the wall under the action of fluid velocity streaks (Wang et al., 2020), with the particles more likely to stay in low-speed

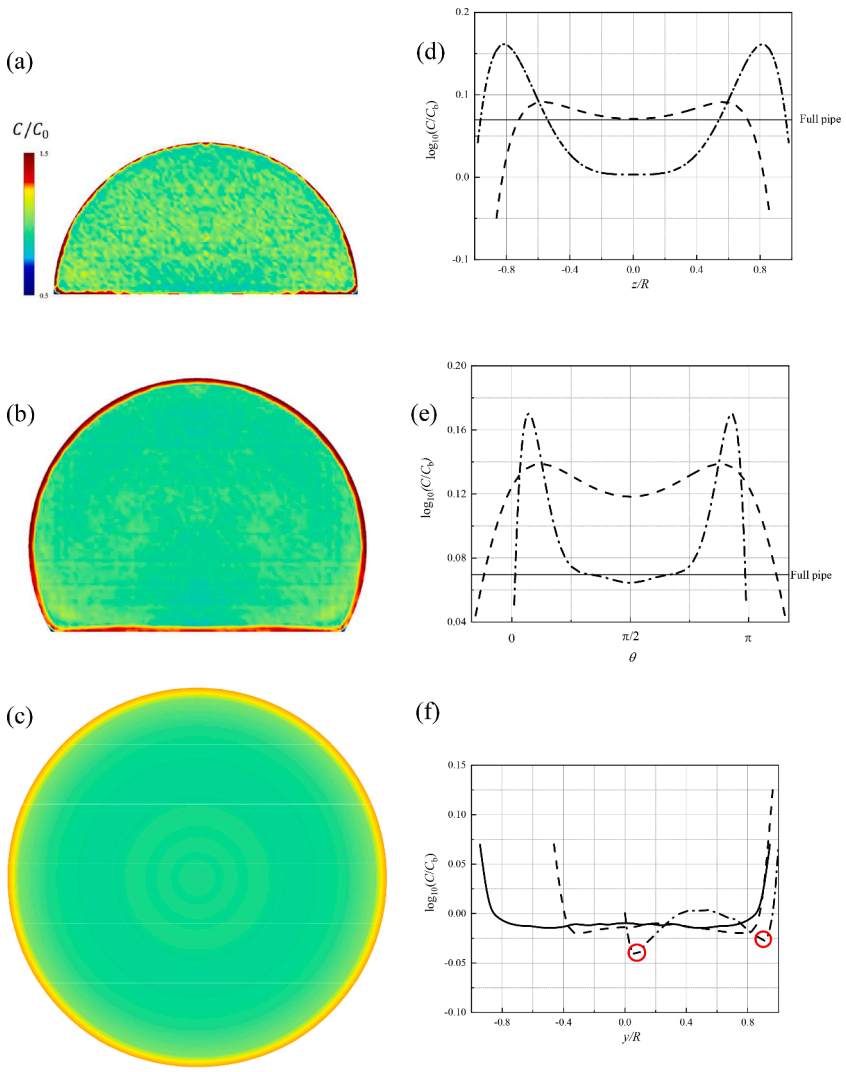

Fig. 12. Average normalized particle concentration in the pipe cross-section. (a-c) contours of the mean particle concentration, $\log_{10}(C/C_b)$, and its profiles (d) along the floor, (e) along the upper wall at $\Delta^+ = 10$ and (f) at $z = 0$ along the centre line. Solid lines: full pipe; dashed lines: three-quarter pipe; dash dot lines: half pipe. The particle concentration in the half pipe has a local minimum at $\Delta^*\approx0.04$ ($\Delta^+\approx30$) indicated by red circles.

streak regions. For larger *St* particles, the high momentum of the particles cannot be dissipated by the action of the low-speed streaks because of their inertia. Therefore, the streak distribution of particles disappears with increases in Stokes number. In addition, for cases with smaller Stokes number, such as the particles studied in this work, the streak structure is not formed near the wall.

Small *St* particles will be slowed down rapidly as they pass through a low-speed streak due to their low inertia. As a result, the particles will accumulate in these regions. However, the position of the velocity streaks is not constant, moving and evolving as the fluid moves along the pipe, and streaks at given locations appear and disappear. In this way, during the evolution of the high- and low-speed streaks, small tracer particles evolve their concentration distribution together with that of the fluid flow, and stable particle streaks are not formed. On the horizontal plane at the centre of the pipes there is clearly no streak structure, therefore a coherent structure within the particles does not appear here either.

By calculating the particle fluxes J_{res} and J_{dep} (particles moving from the wall and towards the wall, respectively), the migratory behaviour of particles can be quantitatively described by the resuspension and deposition rates:

$$v_{res} = J_{res}/C_b \tag{11}$$

$$v_{dep} = J_{dep}/C_b \tag{12}$$

Here, we calculate J_{res} and J_{dep} by counting the number of particles each timestep moving across a boundary at wall distance Δ^+, either away from the wall or towards the wall respectively. Fig. 14 shows the deposition and resuspension rates of particles, normalized by u_{b}, near the upper curved wall and simulated bed of the half and three-quarter pipes at $\Delta^+ = 10$, which was chosen to ensure enough statistical data could be gathered through particle migration events, while also remaining within the turbulent near-wall regions. The straight horizontal line in the figure gives equivalent rates for the full pipe. As shown in Fig. 14, the deposition and resuspension rates of both the half and three-quarter pipes are much lower than that of the full pipe. Because of the larger wall unit, the number of particles within $\Delta^+ = 10$ for the full pipe is more than that in either of the pipes with beds, as is the particle flux. For the half and three-quarter pipes, the deposition and resuspension behaviour of particles near the wall reflects the action of the secondary flows on them.

In Fig. 14(a), for the upper wall of the half pipe, the deposition and resuspension rates of the particles in the centre of the wall remains relatively stable with the same approximate magnitude. The deposition rate of particles decreases from the centre of the wall to the corners,

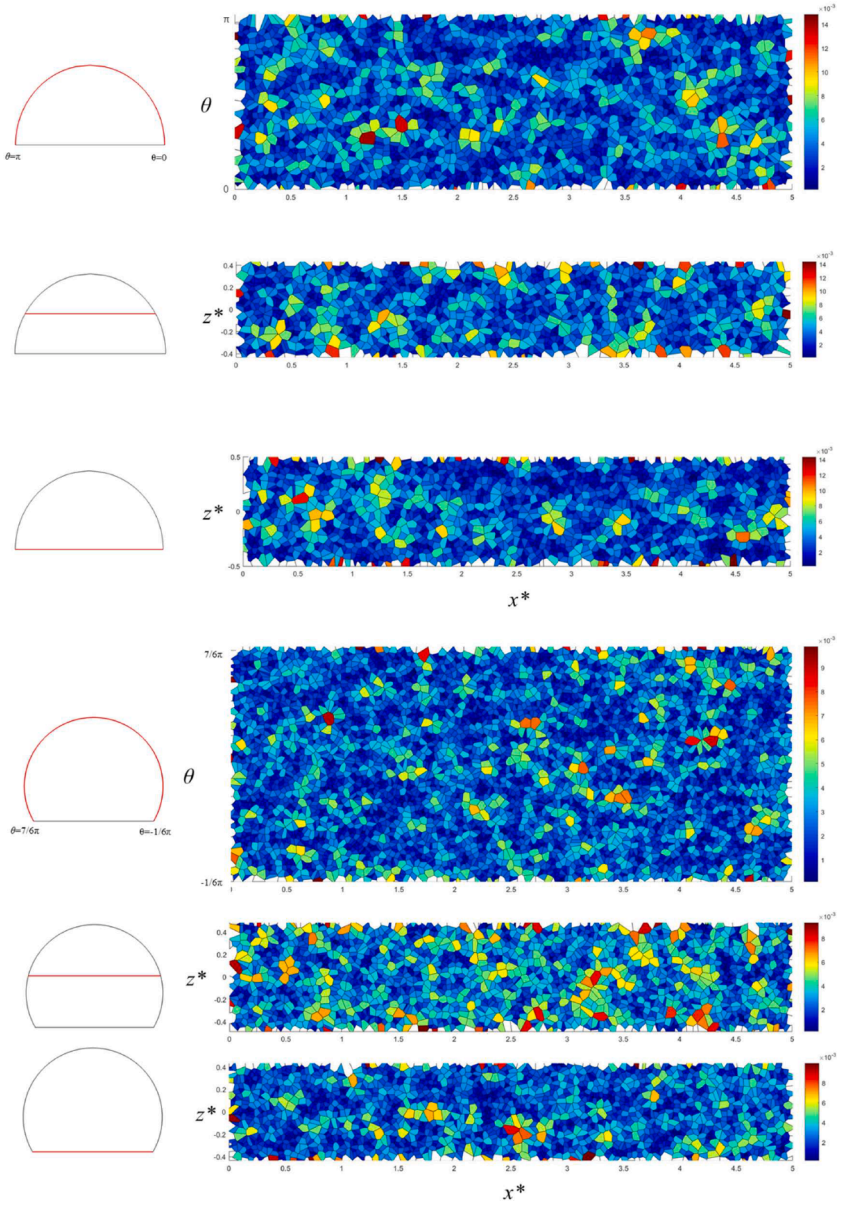

Fig. 13. Voronoi tessellation diagram for particles at sample locations shown on the left, with sampling width $\Delta^+ = 10$. The Voronoi cells are coloured by the area of cells normalized by D^2.

although then is a small maximum near the corners. The resuspension rate of particles follows a similar trend, except that the maximum position near the corners is now further towards the pipe centre. It is worth noting that the maximum value near the corners is smaller than that at the wall centre for both the deposition and resuspension rates.

The maximum values of deposition and resuspension rate near the corners correspond to the movement of particles from the centre of the flow to the corners and back to the centre of the pipe along the pipe wall under the action of the secondary flows, while the deposition and resuspension rates at the centre of the wall represent the movement of particles under the influence of fluid momentum exchange in the boundary layer. Because the turbulence kinetic energy of the flow at the corners is lower and the particles in the corner are restricted by two adjacent walls, the kinetic energy of the particles is more likely to be dissipated. Therefore, regardless of the influence of the secondary flows on particle behaviour, the transport of the particles gradually decreases from the centre of the wall to the corners, and the resuspension and deposition rates also gradually decrease. At the bed of the half pipe, as shown in Fig. 10(b), the deposition rate of particles is similar to that near the upper wall, but there is no resuspension rate maximum near the corners. This is because the vertical component of the cross-stream velocity near the bed is small, while near the upper wall, the secondary flows do not completely flow along the wall, and there is an inward velocity component at $\theta = 1/8\pi$ and $\theta = 7/8\pi$ (Fig. 6(a-b)).

For the three-quarter pipe, the deposition and resuspension rate of the particles near the upper wall is different from that of the half pipe. In the centre of the upper wall, both remain relatively constant and roughly equal. However, there is no maximum in the deposition and resuspension rate near the corners. On the contrary, there is a minimum in these rates followed by an increase into the corners. Obviously, the difference in particle behaviour is related to the different secondary flow characteristics in the two pipes. The secondary flows near the upper wall of the three-quarter pipe occupy less space and are weaker than in the half pipe, so they only slightly affect the movement of particles near the corners. As shown in the figure, the deposition rate of particles near the corners is greater than the resuspension rate, as is the case for particles near the upper wall of the half pipe.

The deposition and resuspension rate of particles near the bed of this

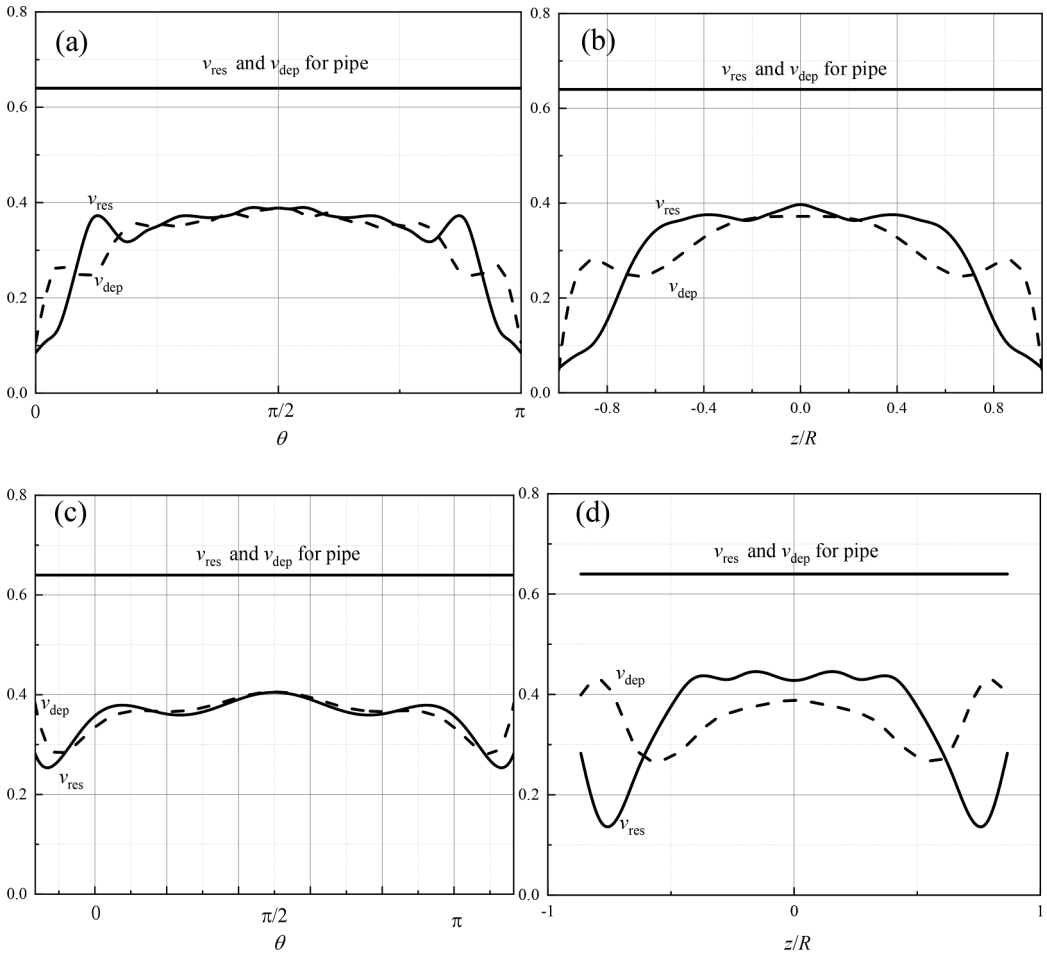

Fig. 14. Deposition and resuspension rates of particles near the (a) and (c) upper curved wall and (b) and (d) bed at $\Delta^+ = 10$. (a) and (b) half pipe; (c) and (d) three-quarter pipe.

pipe is also different from that in the half pipe. The deposition rate in the three-quarter pipe increases close to the corners and is higher than at the centre of the wall. This is because the fluid in this pipe has a larger vertical velocity component when it moves towards the corners compared with the half pipe. Therefore, the secondary flow has a greater effect on the deposition and resuspension rate of particles. The particle resuspension rate also has a minimum value near the corners under the action of the secondary flows. The increase in the resuspension rate at the corners themselves is likely related to the secondary flows near the side wall.

Finally, it is important to note that the rotational symmetry of the full pipe means that the deposition and resuspension rates are isotropic. Furthermore, since these are calculated after concentration profiles have stabilized, there is no net migration towards or away from the wall, hence the two rates are almost identical throughout.

4. Conclusions

Bed formation through particle deposition in pipes is common in many industrial applications. In this work, the bed formed by particle deposition was simplified and modelled assuming that it was flat, horizontal and unchanged in the streamwise direction. Based on this, pipes with two bed heights were considered, with $H_b = 0.5R$ (three-quarter pipe) and R (half pipe), as well as a full pipe used as a touchstone for comparison with the computations of flows in pipes with simulated beds. One-way coupling between the fluid flow and the particles was assumed in order to focus the study on the influence of the secondary flows on the particles and eliminate the complexities introduced by other factors.

The open-source direct numerical simulation code Nek5000 was to calculate the flow in these pipes. The mass flow in the various pipes was assumed to be constant. Therefore, for the full, three-quarter and half pipe, the bulk Reynolds numbers were 5300, 5909 and 7494, respectively, and corresponding shear Reynolds numbers based on the equivalent diameter of the pipes were 360, 401 and 509, respectively. The flow field and particle distribution in the full pipe was shown to be in good agreement with other simulations available in the literature data.

The presence of a simulated sedimentary bed at the bottom of the pipe caused the formation of mean secondary flows in the pipe cross-section. The pattern of these flows was such that there were two streamwise vortices near each corner in the pipe, formed at the junction of the upper curved pipe wall and the flat bed, which transport momentum from the centre of the pipe to the corners. The characteristics of the secondary flows were related to the height of the bed. For $H_b = 0.5R$, the vortices near the bed occupy the space below a line bisecting the corner, with the vortices compressed into the corner. When the bed height was R, the vortices in the lower regions of the pipe were again largely below the corner bisector, but extended vertically above this bisector. The secondary flow intensity near the upper curved wall was always much smaller than that near the pipe floor, although the difference in bed height had a significant impact on the pattern of the secondary flows. It was concluded that the curved boundary inhibits the development of the secondary flow in the upper regions of the pipe, and this effect is related to the flow Reynolds number.

After the full development of the turbulent flow, particles of the same size were added to the three pipes. The Stokes number of the particles in

the full, three-quarter and half pipes were 0.5, 1.2 and 1.9 respectively. The movement of particles in the cross-sectional plane was consistent with that of the secondary flows, but with slightly lower velocities, and results showed that the particle concentration had a maximum value near the curved wall and the simulated beds, the presence of which had a profound effect. In regions near the wall away from the pipe corners, particle concentration in the half pipe was lower than in the three-quarter pipe, caused by its thinner boundary layer. This was reversed for concentration maxima near the pipe corners because of the magnitude of the secondary flows. The secondary flows also changed the deposition and resuspension rate of the particles, particularly near the pipe corners, but these were always less than equivalent rates in the full pipe flow, likely caused by the magnitude of the wall unit.

CRediT authorship contribution statement

Min Liu: Conceptualization, Data curation, Formal analysis, Investigation, Methodology, Project administration, Software, Validation, Visualization, Writing – original draft, Writing – review & editing. **Lee F. Mortimer:** Conceptualization, Data curation, Formal analysis, Investigation, Methodology, Project administration, Software, Validation, Visualization, Writing – original draft, Writing – review & editing. **Bisrat Wolde:** Data curation, Formal analysis, Investigation, Methodology, Software, Validation, Visualization, Writing – original draft, Writing – review & editing. **Michael Fairweather:** Conceptualization, Formal analysis, Investigation, Methodology, Project administration, Supervision, Validation, Visualization, Writing – original draft, Writing – review & editing. **Yanlin Zhao:** Funding acquisition, Supervision, Writing – original draft, Writing – review & editing. **Jun Yao:** Funding acquisition, Supervision, Writing – original draft, Writing – review & editing.

Declaration of Competing Interest

The authors declare the following financial interests/personal relationships which may be considered as potential competing interests: Min Liu reports financial support was provided by National Natural Science Foundation of China. Min Liu reports financial support was provided by High-end Foreign Experts Recruitment Plan of China.

Data availability

Data will be made available on request.

Acknowledgements

This work was supported by the National Natural Science Foundation of China (No. 51876221) and the High-end Foreign Expert Introduction Project (G20190001270; B18054). The authors also gratefully acknowledged the financial support from the China Scholarship Council.

References

Alassar, R.S., 2014. Fully developed forced convection through semicircular ducts. J. Thermophys. Heat Tr. 28, 560–565.
Armenio, V., Fiorotto, V., 2001. The importance of the forces acting on particles in turbulent flows. Phys. Fluids 13, 2437–2440.
Arolla, S.K., Desjardins, O., 2015. Transport modeling of sedimenting particles in a turbulent pipe flow using Euler-Lagrange large eddy simulation. Int. J. Multiph. Flow 75, 1–11.
Bradshaw, P., 1987. Turbulent secondary flows. Annu. Rev. Fluid Mech. 19, 53–74.
Brundrett, E., Baines, W.D., 1964. The production and diffusion of vorticity in duct flow. J. Fluid Mech. 19, 375–394.
El Hasadi, Y.M.F., Busedra, A.A., Rustum, I.M., 2007. Laminar mixed convection in the entrance region of horizontal semicircular ducts with the flat wall at the top. J. Heat Trans.-T ASME 129, 1203–1211.
El Khoury, G.K., Schlatter, P., Noorani, A., Fischer, P.F., Brethouwer, G., Johansson, A.V., 2013. Direct numerical simulation of turbulent pipe flow at moderately high Reynolds numbers. Flow Turbul. Combust. 91, 475–495.
Elghobashi, S., 1994. On predicting particle-laden turbulent flows. Appl. Sci. Res. 52, 309–329.
Esmaily, M., Villafañe, L., Banko, A.J., Iaccarino, G., Eaton, J.K., Mani, A., 2020. A benchmark for particle-laden turbulent duct flow: A joint computational and experimental study. Int. J. Multiphas. Flow 132, 103410.
Fischer, P. F., Lottes, J. W., and Kerkemeier, S. G., "Nek5000," http://nek5000.mcs.anl.gov (2008).
Flack, R., and Brun, K., "Fundamental analysis of the secondary flows and jet-wake in a torque converter pump: Part 2 - Flow in a curved stationary passage and combined flows," in Proceedings ASME/JSME 2003 4th Joint Fluids Summer Engineering Conference (2003).
Gavrilakis, S., 1992. Numerical simulation of low-Reynolds-number turbulent flow through a straight square duct. J. Fluid Mech. 244, 101–129.
Hurst, K.S., Rapley, C.W., 1991. Turbulent flow measurements in a 30/60 degree right triangular duct. Int. J. Heat Mass Tran. 34, 739–748.
Huser, A., Biringen, S., 1993. Direct numerical simulation of turbulent flow in a square duct. J. Fluid Mech. 257, 65–95.
Jimenez, J., Hoyas, S., 2008. Turbulent fluctuations above the buffer layer of wall-bounded flows. J. Fluid Mech. 611, 215–236.
Kuerten, J.G.M., 2016. Point-particle DNS and LES of particle-laden turbulent flow – A state-of-the-art review. Flow Turbul. Combust. 97, 689–713.
Larsson, I.A.S., Lindmark, E.M., Lundström, T.S., Nathan, G.J., 2011. Secondary flow in semi-circular ducts. J. Fluid Eng.-T ASME 133, 101206.
Lin, Z.-W., Shao, X.-M., Yu, Z.-S., Wang, L.-P., 2017. Effects of finite-size heavy particles on the turbulent flows in a square duct. J. Hydrodyn. 29, 272–282.
Lin, Z., Yu, Z., Shao, X., Wang, L.-P., 2017a. Effects of finite-size neutrally buoyant particles on the turbulent flows in a square duct. Phys. Fluids 29, 103304.
Liou, T.-M., Chen, C.-C., Chen, M.-Y., 2003. Rotating effect on fluid flow in two smooth ducts connected by a 180-degree bend. J. Fluid Eng.-T ASME 125, 138–148.
Liu, M., Yao, J., Zhao, Y., 2021a. Particle dispersion in turbulent sedimentary duct flows. Adv. Powder Tech. 32, 4245–4262.
Liu, M., Yao, J., Zhao, Y.-L., 2021b. The dispersion of particles in turbulent semi-circular duct flows. Pet. Sci. 18, 1240–1255.
Madabhushi, R.K., Vanka, S.P., 1991. Large eddy simulation of turbulence-driven secondary flow in a square duct. Phys. Fluids A 3, 2734–2745.
Marin, O., Vinuesa, R., Obabko, A.V., Schlatter, P., 2016. Characterization of the secondary flow in hexagonal ducts. Phys. Fluids 28, 125101.
Maxey, M.R., Riley, J.J., 1983. Equation of motion for a small rigid sphere in a nonuniform flow. Phys. Fluids 26, 883–889.
Mortimer, L.F., Njobuenwu, D.O., Fairweather, M., 2019. Near-wall dynamics of inertial particles in dilute turbulent channel flows. Phys. Fluids 31, 063302.
Nikitin, N., Yakhot, A., 2005. Direct numerical simulation of turbulent flow in elliptical ducts. J. Fluid Mech. 532, 141–164.
Nikuradse, J., 1930. Turbulent strömung in nicht kreisförmigen rohren. Ing. Arch. 1, 306–332.
Noorani, A., Sardina, G., Brandt, L., Schlatter, P., 2016. Particle transport in turbulent curved pipe flow. J. Fluid Mech. 793, 248–279.
Noorani, A., Vinuesa, R., Brandt, L., Schlatter, P., 2016a. Aspect ratio effect on particle transport in turbulent duct flows. Phys. Fluids 28, 115103.
Pan, Y., Banerjee, S., 1996. Numerical simulation of particle interactions with wall turbulence. Phys. Fluids 8, 2733–2755.
Pinelli, A., Uhlmann, M., Sekimoto, A., Kawahara, G., 2010. Reynolds number dependence of mean flow structure in square duct turbulence. J. Fluid Mech. 644, 107–122.
Pirozzoli, S., Modesti, D., Orlandi, P., Grasso, F., 2018. Turbulence and secondary motions in square duct flow. J. Fluid Mech. 840, 631–655.
Prandtl, L., "Über die ausgebildete turbulenz," in Proceedings 2nd International Congress Applied Mechanics (1926).
Rani, S.L., Winkler, C.M., Vanka, S.P., 2004. Numerical simulations of turbulence modulation by dense particles in a fully developed pipe flow. Powder Technol. 141, 80–99.
Rice, H.P., Fairweather, M., Hunter, T.N., Peakall, J., Biggs, S.R., 2017. The influence of relative fluid depth on initial bedform dynamics in closed, horizontal pipe flow. Int. J. Multiph. Flow 93, 1–16.
Robinson, S.K., 1991. Coherent motions in the turbulent boundary layer. Annu. Rev. Fluid Mech. 23, 601–639.
Schiller, L., Naumann, A., 1933. Fundamental calculations in gravitational processing. Z. Ver. Dtsch. Ing. 77, 318–320.
Sharma, G., Phares, D.J., 2006. Turbulent transport of particles in a straight square duct. Int. J. Multiph. Flow 32, 823–837.
Sherik, A. M., Zaidi, S. R., Tuzan, E. V., and Perez, J. P., "Black powder in gas transmission systems," in Proceedings Conference on CORROSION (2008).
Vinuesa, R., Noorani, A., Lozano-Durán, A., El Khoury, G.K., Schlatter, P., Fischer, P.F., Nagib, H.M., 2014. Aspect ratio effects in turbulent duct flows studied through direct numerical simulation. J. Turbul. 15, 677–706.
Vinuesa, R., Prus, C., Schlatter, P., Nagib, H.M., 2016. Convergence of numerical simulations of turbulent wall-bounded flows and mean cross-flow structure of rectangular ducts. Meccanica 51, 3025–3042.
Vreman, A.W., 2007. Turbulence characteristics of particle-laden pipe flow. J. Fluid Mech. 584, 235–279.
Wang, Y., Fairweather, M., Mortimer, L.F., Zhao, Y., Yao, J., 2020. Mechanisms of particle preferential concentration induced by secondary motions in a dilute turbulent square duct flow. Phys. Fluids 32, 123313.

Wang, J., Li, Y., Zhao, J., Shi, B., Gong, J., Li, Q., 2022. Simulation of the effect of hydrate adhesion properties on flow safety in solid fluidization exploitation. Petroleum in press.
Winkler, C.M., Rani, S.L., 2009. Relative importance of the lift force on heavy particles due to turbulence driven secondary flows. Powder Technol. 190, 310–318.
Yao, J., Fairweather, M., 2010. Inertial particle resuspension in a turbulent, square duct flow. Phys. Fluids 22, 033303.
Yao, J., Fairweather, M., 2012. Particle deposition in turbulent duct flows. Chem. Eng. Sci. 84, 781–800.
Zeng, L., Najjar, F., Balachandar, S., Fischer, P., 2009. Forces on a finite-sized particle located close to a wall in a linear shear flow. Phys. Fluids 21, 033302.
Zhang, G., Li, J., Yang, H., Liu, G., Pang, Q., Wu, T., Huang, H., 2022. Simulation research on solid fluidization exploitation of deepwater superficial layer natural gas hydrate reservoirs based on double-layer continuous pipe. J. Nat. Gas Sci. Eng. 108, 104828.